AGU PUBLICATIONS

JGR

Journal of Geophysical Research: Atmospheres

RESEARCH ARTICLE
10.1002/2015JD024241

Three-dimensional modeling of the mixing state of particles over Greater Paris

Shupeng Zhu[1], Karine Sartelet[1], Yang Zhang[2], and Athanasios Nenes[3,4,5,6]

[1]CEREA, Joint Laboratory Ecole des Ponts ParisTech–EDF R and D, Université Paris-Est, Champs-sur-Marne, France, [2]Department of Marine, Earth, and Atmospheric Science, North Carolina State University, Raleigh, North Carolina, USA, [3]School of Earth and Atmospheric Sciences, Georgia Institute of Technology, Atlanta, Georgia, USA, [4]School of Chemical and Biomolecular Engineering, Georgia Institute of Technology, Atlanta, Georgia, USA, [5]Institute of Chemical Engineering Sciences (ICE-HT), Foundation for Research and Technology, Patras, Greece, [6]Institute for Environmental Research and Sustainable Development, National Observatory of Athens, Palea Penteli, Greece

Key Points:
- More than half of black carbon particles are barely mixed at the urban site of Paris
- Mixing state-resolved simulation leads to higher nitrate and lower ammonium in the particulate phase over Greater Paris in summer 2009
- The mixing state assumption made in air quality models strongly affects aerosols optical properties and CCN activation

Correspondence to:
S. Zhu,
shupeng.zhu@enpc.fr

Citation:
Zhu, S., K. Sartelet, Y. Zhang, and A. Nenes (2016), Three-dimensional modeling of the mixing state of particles over Greater Paris, *J. Geophys. Res. Atmos.*, *121*, 5930–5947, doi:10.1002/2015JD024241.

Received 18 SEP 2015
Accepted 12 APR 2016
Accepted article online 3 MAY 2016
Published online 28 MAY 2016

Abstract A size-composition resolved aerosol model (SCRAM) is coupled to the Polyphemus air quality platform and evaluated over Greater Paris. SCRAM simulates the particle mixing state and solves the aerosol dynamic evolution taking into account the processes of coagulation, condensation/evaporation, and nucleation. Both the size and mass fractions of chemical components of particles are discretized. The performance of SCRAM to model air quality over Greater Paris is evaluated by comparison to $PM_{2.5}$, PM_{10}, and Aerosol Optical Depth (AOD) measurements. Because air quality models usually assume that particles are internally mixed, the impact of the mixing state on aerosols formation, composition, optical properties, and their ability to be activated as cloud condensation nuclei (CCN) is investigated. The simulation results show that more than half (up to 80% during rush hours) of black carbon particles are barely mixed at the urban site of Paris, while they are more mixed with organic species at a rural site. The comparisons between the internal-mixing simulation and the mixing state-resolved simulation show that the internal-mixing assumption leads to lower nitrate and higher ammonium concentrations in the particulate phase. Moreover, the internal-mixing assumption leads to lower single scattering albedo, and the difference of aerosol optical depth caused by the mixing state assumption can be as high as 72.5%. Furthermore, the internal-mixing assumption leads to lower CCN activation percentage at low supersaturation, but higher CCN activation percentage at high supersaturation.

1. Introduction

Airborne particulate matter (PM) is regulated in many countries due to its adverse impact on human health, visibility, and climate [*Pascal et al.*, 2013; *Davidson et al.*, 2005; *Jacobson*, 2002b]. Hence, air quality models are used to simulate and forecast its concentration. Most of existing models assume that particles are internally mixed (i.e., all particles of the same size range and in the same grid cell have the same chemical composition), largely for computational reasons. However, field measurements [*Murphy et al.*, 2006; *Healy et al.*, 2012] have proved that a wide range of particle compositions can coexist in the atmosphere, namely, particles could have a great variety of mixing states, and the internal-mixing assumption may be inaccurate especially close to emission sources. For example, the measurements of *Healy et al.* [2012] showed that particles from different sources may have different compositions, and particles with local or transported origins have distinct mixing states [*Healy et al.*, 2013]. The mixing state of particles may influence aerosol properties, such as absorption and scattering properties [*Lesins et al.*, 2002; *Mallet et al.*, 2004], as well as the global radiative forcing [*Jacobson*, 2001]. By influencing the particle composition, the mixing state also influences the hygroscopicity and the potential of particles to be activated as cloud condensation nuclei [*Wex et al.*, 2010; *Lance et al.*, 2013; *Leck and Svensson*, 2014].

Models of different complexities have been developed, in order to represent the particle mixing state and its evolution due to aerosol dynamics (coagulation and condensation/evaporation). The most accurate approach is to track the mixing state of individual particles, such as in the particle-resolved aerosol model of *Riemer et al.* [2009]. Although this approach is accurate and takes into account all processes related to aerosol dynamics, it is computationally expensive for large-scale 3-D simulations because it explicitly represents the mixing state

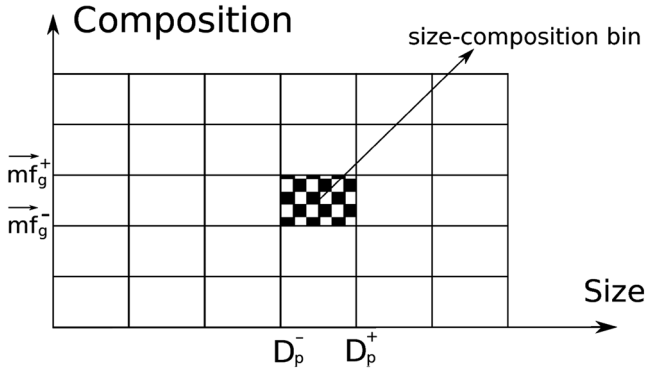

Figure 1. Aerosol section representation used in the SCRAM model. Particles are discretized based on both its size (diameter D_p) and its composition (defined by the mass fraction (mf) of each chemical group (g) within the particle).

on a per-particle level. To be more computational efficient for 3-D simulations, approaches with a modal discretization of the size distribution of particles have been developed. The particle mixing state is represented by using separated lognormal modes to represent different particle populations [*Stier et al.*, 2005; *Bauer et al.*, 2008; *Vogel et al.*, 2009; *Aquila et al.*, 2011]. However, the accuracy of the modal approach is limited by the characteristics of the predefined modes. The representation of the particle mixing state is limited in existing modal models, as most of them only separate particle populations between soluble/insoluble and mixed/not mixed. For example, in the recent work of *Kaiser et al.* [2014], only nine modes are available in the whole size range to host different particle mixing states. More sophisticated treatments of the particle mixing state have been used in the source-oriented model of *Kleeman and Cass* [2001], where each source is associated to an aerosol distribution, which interacts with the gas phase by condensation/evaporation. Coagulation between different distributions is added to the model in the follow-up work of *Zhang et al.* [2014], but all coagulated particles are lumped into a single population and their source identity is lost. Another problem of the source-oriented approach is that it may not be able to separate aged particles from flash emitted ones if they come from the same source, as they would be identified as the same population. To represent the particle mixing state independently of their sources, *Jacobson et al.* [1994] and *Russell and Seinfeld* [1998] introduced mixing-state-resolved (MSR) subpopulations to separate mixed particles from particles of pure chemical substances, in the sectional discretization of the size distribution of particles. *Jacobson* [2002a] expanded on *Jacobson et al.* [1994] by allowing particles to have different mass fractions. By discretizing the mass fractions, *Lu and Bowman* [2010] used a threshold mass fraction to define whether a chemical species is mixed or not. Similarly, *Oshima et al.* [2009] and *Matsui et al.* [2014] represent the particle mixing state by discretizing into sections both the size distribution and the mass fraction of black carbon. Extended from the discretization scheme of *Dergaoui et al.* [2013], which discretizes the size distribution and the mass fractions of chemical components, the Size-Composition Resolved Aerosol Model (SCRAM) [*Zhu et al.*, 2015] solves the aerosol dynamic evolution under different mixing states (mixing state resolved) taking into account the processes of coagulation, condensation/evaporation, and nucleation.

In this work, the SCRAM model is integrated into the Polyphemus air quality modeling platform, and its performance to model air quality over Greater Paris is evaluated by comparisons to $PM_{2.5}$, PM_{10}, and Aerosol Optical Depth (AOD) measurements. The impact of the mixing state assumption on aerosol formation, composition as well as on aerosol optical properties and ability to be activated as cloud condensation nuclei is investigated.

2. Model Description and Simulation Setup

SCRAM uses a 2-D sectional structure as shown in Figure 1, where particles are discretized based on both size and composition. Each size section is limited by an upper bound diameter D_p^+ and a lower bound diameter D_p^-. Composition sections are defined by first identifying chemical groups, which may contain one or several chemical species, and then by discretizing the mass fraction (mf) of each chemical group into sections of bounds mf^- and mf^+. These sections are combined to form the different particle compositions. For example, if five chemical groups (A, B, C, D, and E) are included in a simulation, as in this work, then each composition section corresponds to mass fraction sections defined for the first four chemical groups ($[mf_A^-, mf_A^+]$, $[mf_B^-, mf_B^+]$, $[mf_C^-, mf_C^+]$, $[mf_D^-, mf_D^+]$). The mass fraction of the last chemical group is not discretized but computed by mass conservation. The generation of composition sections is automatic, by screening all combinations of mass fraction sections of each chemical group based on a rule that the sum of the lower bounds of mass fraction sections within the particle is no more than 100%. During the simulation, the mass of each chemical species and the particle number are tracked within each size-composition section of this 2-D sectional structure.

Those information are used to compute the average diameter and the mass fraction of each chemical group in order to position the section into the appropriate size-composition section.

Three aerosol dynamic processes are taken into account in SCRAM: coagulation, condensation/evaporation, and nucleation. The parameterization of *Vehkamäki et al.* [2002] for the homogeneous binary nucleation of sulphate and water can be used to simulate nucleation. For coagulation, the collisions of particles caused by Brownian motion is simulated using the module developed by *Dergaoui et al.* [2013]. Three different approaches may be used in SCRAM for condensation/evaporation: the fully dynamic approach, the bulk equilibrium approach, or the hybrid approach. The fully dynamic approach computes the mass transfer rate due to condensation/evaporation for each particle size and composition section. It is the most accurate method among the three approaches, but it has the highest computational cost. The bulk equilibrium approach computes the mass partitioning between the gas and the bulk particle concentrations by assuming instantaneous thermodynamic equilibrium. After this bulk condensation/evaporation, the bulk particle concentration is redistributed between the particle sections. The bulk equilibrium approach is more computationally efficient than the dynamic approach, but it is less accurate, because particles may not be at thermodynamic equilibrium with their surrounding and the composition identity of each particle is not considered during the computation. Finally, the hybrid approach [*Debry and Sportisse*, 2006] provides a compromise by assuming bulk equilibrium for small particles (e.g., $D_p \leq 0.1\mu m$) while dynamically computing the mass transfer rate for large particles (e.g., $D_p > 0.1\mu m$). In this work, after condensation/evaporation, the moving center algorithm is used for mass number redistribution among fixed size sections. More details about the discretization method, the mathematical derivation, and model validations can be found in *Zhu et al.* [2015].

SCRAM has been integrated into the Polair3D air quality model [*Sartelet et al.*, 2007] of the Polyphemus air quality platform [*Mallet et al.*, 2007] for 3-D simulations over the Paris area. The Carbon Bond 05 model (CB05) [*Sarwar et al.*, 2008] is used for gas-phase chemistry. The thermodynamic model used for condensation/evaporation of inorganic aerosols is ISORROPIA [*Nenes et al.*, 1998], while the H^2O model [*Couvidat et al.*, 2012] is used for secondary organic aerosol (SOA) formation. Although the condensation/evaporation of inorganics may be computed dynamically, bulk equilibrium is always assumed for organics, because a dynamic approach is not available in H^2O. For in-cloud processing of aerosols, the VSRM model [*Fahey and Pandis*, 2001] is used.

The Polair3D/Polyphemus air quality model was modified to take into account both size and composition sections. The number of particles and the chemical components of each size/composition sections are transported. For input data, both initial and boundary conditions of the simulation can be specified as internally mixed (data without composition information) or mixing state resolved (data with composition information). In case of internally mixed data, the composition index of each section is computed based on the composition of particles in that section. Emissions are considered as not mixed (particles are only made of the emitted chemical component). Simulations in this work assume that initial and boundary conditions are internally mixed as they are obtained from a larger-scale simulation, which assumes that particles are internally mixed.

The simulation domain is the same as in *Couvidat et al.* [2013] and *Wang et al.* [2014]. As shown in Figure 2, it covers the Paris area ([1.2°E, 3.5°E] × [47.9°N, 50.1°N]) with a horizontal resolution of 0.02° × 0.02°, and nine layers vertically from the ground to 12 km. The meteorology data are obtained from the Weather Research and Forecasting (WRF) version 3.6 [*Skamarock et al.*, 2005] model using an urban canopy model and the Corine land use database [*Kim et al.*, 2013] with the YSU parameterization [*Hong et al.*, 2006] for the planetary boundary layer. Initial and boundary condition inputs for aerosols and gas are from *Couvidat et al.* [2013], which were obtained from nested simulations over Europe and France. The initial and boundary conditions for the Europe simulation were obtained from the Model for OZone And Related chemical Tracers (Mozart v2.0) [*Horowitz et al.*, 2003], and those for the France simulation were obtained from the Europe simulation, as detailed in [*Couvidat et al.*, 2013; *Wang et al.*, 2014]. Biogenic VOC emissions are generated from the MEGAN emission model [*Guenther et al.*, 2006], while anthropogenic emissions of gases and particles are obtained from the Airparif inventory [*Airparif*, 2010]. Following *Couvidat et al.* [2012], semivolatile organic compound (SVOC) emissions are estimated by multiplying primary organic aerosol (POA) emissions by a factor of 5, and SVOC are represented by three molecules depending on their volatility POAlP, POAmP, and POAhP, which represent respectively 25%, 32%, and 43% of SVOC emissions. All SVOC are emitted in the gas phase and partition between the gas and the particle phases. Other emitted species are black carbon and dust, which are emitted as pure BC and pure dust, respectively. Four simulations are carried out for 1 week from 28 June

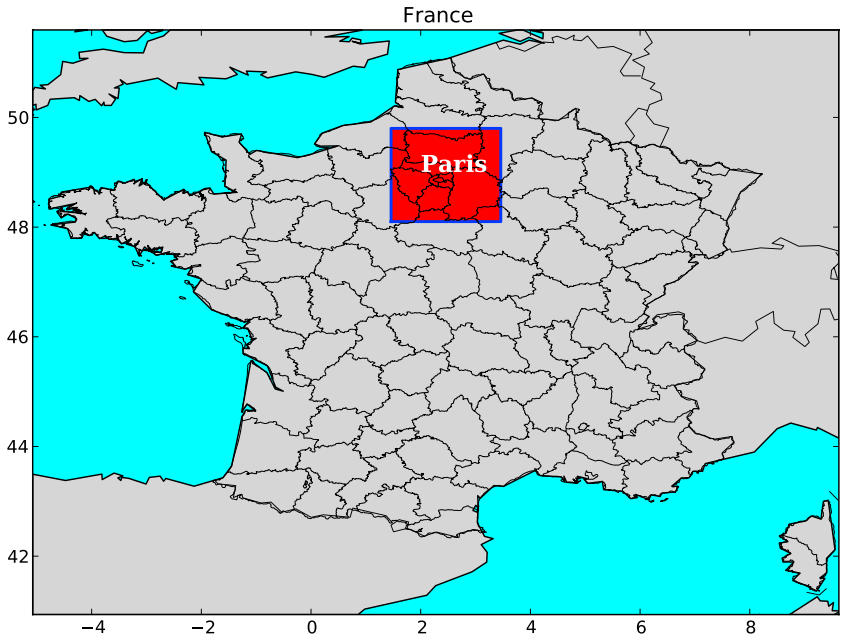

Figure 2. Simulated domain located within the red rectangle.

to 5 July 2009 on a Dell server equipped with two Bi-Xeon E5-2680v2 CPU (10 cores 2.8 GHz) and 64 GB RAM. The first two simulations assume that particles are internally mixed (IM), while the other two are mixing state-resolved (MSR) simulations. Within each of the two groups of simulations, one simulation uses the fully dynamic approach for condensation/evaporation, while the other one uses the bulk equilibrium approach for solving condensation/evaporation.

The size distribution is discretized into five size sections between 0.01 and 10 μm with section bounds of 0.01 μm, 0.0398 μm, 0.1585 μm, 0.6310 μm, 2.5119 μm, and 10.0 μm. As in *Zhu et al.* [2015], 31 aerosol species are grouped into five groups: inorganic hydrophilic (IL), organic hydrophilic (OL), organic hydrophobic (OB), black carbon (BC), and dust (DUST). Such aggregation is made mostly based on the optical and hygroscopic properties of the 31 species. BC is put in a single group, because of its strong correlation to traffic emission, its unique absorption optical characteristic, and its hydrophobic nature. Dust is put into the last group (the mass fraction is not discretized), as the mixing state of dust is not the focus of this paper. The five inorganic species (sodium, sulphate, nitrate, ammonium, and chloride) are grouped together into IL as all of them are hydrophilic. Finally, the 23 organic species are separated into OL and OB based on their hygroscopic characteristics [*Couvidat et al.*, 2012]. For the MSR simulations, the mass fraction of each of the first four groups (IL, OL, OB, and BC) is discretized into three mass fraction sections ([0.0, 0.2], [0.2, 0.8], [0.8, 1.0]). A total of 20 possible particle compositions are generated, as presented in Table 1. As a result, there are a total of 100 size composition sections (20 composition sections × 5 size sections) used in the MSR simulation. DUST is not discretized and its mass fraction is obtained by mass conservation. While in SCRAM the number and bounds of the mass-fraction sections can be arbitrarily chosen, we limited the number of mass fraction sections to three in this study because of computational cost. The 0.2 and 0.8 cutoffs are chosen because five chemical groups are used in this study. If all five groups are equally mixed within a particle, then each of them has a mass fraction equal to 0.2. If the mass fraction of one chemical group is more than 0.2, it is considered as a main component of the particle. If the mass fraction of one chemical group is more than 0.8, then it is considered as a dominating species as the mass fractions of all other species are below 0.2. The names assigned to the particle compositions are chosen depending on the main chemical groups (with mass fractions greater than 20%) of each composition. Particles with more than 80% of one chemical group are considered as barely mixed, they are referred to as DUST, BC, OB, OL, and IL. Besides, BC+, OB+, OM+, OL+, and IL+ represent compositions that are partly mixed as there is not a chemical group that dominates the mass fraction by more than 80%, but only one chemical group has a mass fraction larger than 20%. When both hydrophilic and hydrophobic organics are equally present in the composition, they are referred to as organic matter (OM). In each group, water may also be present, although it is not considered when computing the mass fractions (it is calculated

Table 1. Twenty MSR Particle Compositions

		Mass Fraction of Each Group (%)			
Composition Index	Pseudo Names	IL	OL	OB	BC
1	DUST	0–20	0–20	0–20	0–20
2	BC1+	0–20	0–20	0–20	20–80
3	BC	0–20	0–20	0–20	80–100
4	OB+	0–20	0–20	20–80	0–20
5	OB+BC	0–20	0–20	20–80	20–80
6	OB	0–20	0–20	80–100	0–20
7	OL+	0–20	20–80	0–20	0–20
8	OL+BC	0–20	20–80	0–20	20–80
9	OM+	0–20	20–80	20–80	0–20
10	OM+BC	0–20	20–80	20–80	20–80
11	OL	0–20	80–100	0–20	0–20
12	IL+	20–80	0–20	0–20	0–20
13	IL+BC	20–80	0–20	0–20	20–80
14	IL+OB	20–80	0–20	20–80	0–20
15	IL+OB+BC	20–80	0–20	20–80	20–80
16	IL+OL	20–80	20–80	0–20	0–20
17	IL+OL+BC	20–80	20–80	0–20	20–80
18	IL+OM	20–80	20–80	20–80	0–20
19	IL+OM+BC	20–80	20–80	20–80	20–80
20	IL	80–100	0–20	0–20	0–20

separately with the thermodynamic models). Concerning the size distribution of emitted particles, pure BC particles are emitted into the first four size sections (lowest diameters), while pure dust particles are emitted into the last four size sections (highest diameters). The same method as *Sartelet et al.* [2007] was used to define the size distribution for BC and dust emissions, 9% BC is emitted in the first size section, 25% in the second, and 33% in both the third and fourth size sections. While for dust, 77% of dust emission concentrated in the last size section (fifth), 9% in both the third and fourth sections, and only 5% in the second size section.

3. Particle Concentrations

This section analyzes the simulated particle concentrations from all four simulations. First, $PM_{2.5}$ and PM_{10} are compared to observational data. The influences on $PM_{2.5}$ and PM_{10} of the mixing state assumption and of the approach used to model condensation/evaporation (equilibrium versus dynamic) are investigated. Second, as only inorganic concentrations may be computed dynamically, a more specific analysis is performed on inorganic aerosol formation. Finally, the mixing state of BC is studied. Because BC is an inert species and it is emitted by traffic, which is an important source of pollution over Paris, it is a good candidate to demonstrate the ability of SCRAM to study the particle mixing state.

Table 2. Definitions of the Statistics Used in This Work[a]

Statistic indicator	Definition
Correlation	$\frac{\sum_{i=1}^{n}(c_i-\bar{c})(o_i-\bar{o})}{\sqrt{\sum_{i=1}^{n}(c_i-\bar{c})^2}\sqrt{\sum_{i=1}^{n}(o_i-\bar{o})^2}}$
Mean fractional bias (MFB)	$\frac{1}{n}\sum_{i=1}^{n}\frac{c_i-o_i}{(c_i+o_i)/2}$
Mean fractional error (MFE)	$\frac{1}{n}\sum_{i=1}^{n}\frac{\lvert c_i-o_i\rvert}{(c_i+o_i)/2}$

[a] $\{o_i\}_{i=1,n}$ and $\{c_i\}_{i=1,n}$ are the observed and the model concentrations at time i, respectively; n is the number of avaliable observations.

Table 3. Statistics Between Simulation Results and the Measurements of the BDQA (Base de Données Sur la Qualité de l'Air) Network During the MEGAPOLI Summer Experiment[a]

	$PM_{2.5}$					PM_{10}				
Simulations	Obs. Mean ($\mu g\ m^{-3}$)	Sim. Mean ($\mu g\ m^{-3}$)	Corr. (%)	MFB (%)	MFE (%)	Obs. Mean ($\mu g\ m^{-3}$)	Sim. Mean ($\mu g\ m^{-3}$)	Corr. (%)	MFB (%)	MFE (%)
IM-eq	21.35	17.15	56.5	−15.8	32.8	35.54	18.96	36.3	−53.8	59.4
IM-dy	21.35	17.14	56.1	−15.4	32.7	35.54	19.11	34.7	−52.7	58.5
MSR-eq	21.35	17.18	56.5	−15.6	32.7	35.54	18.97	36.2	−53.7	59.3
MSR-dy	21.35	17.42	57.9	−13.9	31.9	35.54	19.35	38.5	−51.6	57.4

[a]Obs., observation; Sim., simulation. Corr., correlation.

3.1. PM Concentrations

The model performance to simulate PM concentration over Greater Paris is evaluated based on the criteria proposed by *Boylan and Russell* [2006]: PM performance goal is met when the mean fractional bias (MFB) is in range of [−30%, 30%] and the mean fractional error (MFE) is in range of [0%, 50%]; the PM performance criterion is met when the MFB is in range of [−60%, 60%] and the MFE is in range of [0%, 75%]. The PM performance goal corresponds to the level of accuracy that is considered to be close to the best level that can be expected to be achieved, while the PM performance criterion corresponds to the level of accuracy that is considered to be acceptable for modeling applications. The correlation coefficient is also used as statistical indicator in this work. Definitions about MFB, MFE, and correlation are detailed in Table 2.

Statistics of the four simulations are presented in Table 3 for both $PM_{2.5}$ and PM_{10}. For all the simulations, the PM performance goal is met for $PM_{2.5}$, and the PM criterion is met for PM_{10}. In other words, the model simulates well $PM_{2.5}$, while PM_{10} is slightly underestimated as expected from the former simulations which use the same setup and input data [*Couvidat et al.*, 2013; *Wang et al.*, 2014]. The reasons for this underestimation of coarse particles may be that resuspension is not modeled and dust boundary conditions may be underestimated.

Although the statistics of the different simulations are very similar, they are always better for the dynamic approach than for the equilibrium approach no matter what mixing assumption is used. Moreover, in general, MSR simulations have better statistics than the IM ones, especially with the dynamic approach, partly because the MSR simulations lead to slightly higher PM concentrations than the IM simulations. This is a consequence of differences of inorganic aerosol concentrations, as discussed in the next section.

The dynamic approach leads to larger differences between the IM and MSR simulations than the equilibrium approach. This can be observed from Figures 3 and 4, where the time evolutions of $PM_{2.5}$ and inorganic

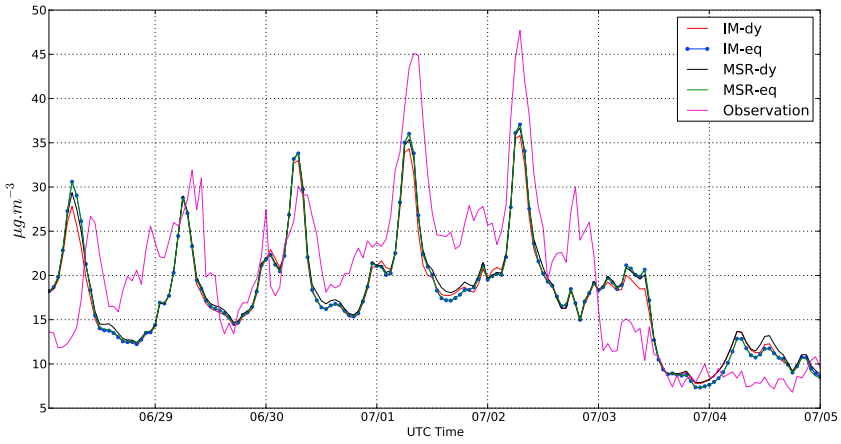

Figure 3. Time evolution of $PM_{2.5}$ at A BDQA site Bobigny (48.90°N, 2.45°E) between 28 June and 5 July 2009 (IM-dy: IM simulation with dynamic approach for C/E process; IM-eq: IM simulation with equilibrium approach for C/E process. MSR-dy: MSR simulation with dynamic approach for C/E process; MSR-eq: MSR simulation with equilibrium approach for C/E process. Observation: ground measurement data).

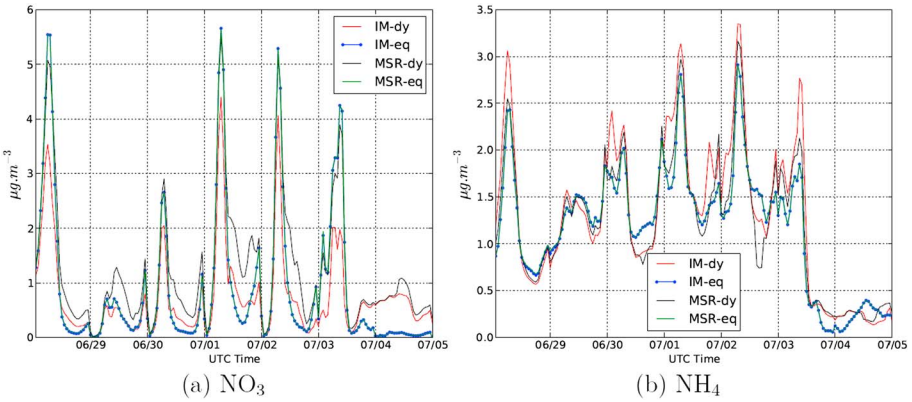

Figure 4. Time evolution of NO_3 and NH_4 at BDQA site Gennevilliers (48.93°N, 2.29°E) between 28 June and 5 July 2009.

concentrations at Bobigny (48.90°N, 2.45°E) (marked in Figure 5), respectively, are presented for the four simulations. The concentrations from the IM and MSR simulations are similar when bulk equilibrium is assumed, because the mass transfer by condensation/evaporation between particles and gas depends on the total bulk mass of inorganic components and it is independent of the mixing state. Condensation/evaporation is the main process leading to differences in the mixing state here, as both IM and MSR simulations have the same initial and boundary concentrations. Furthermore, coagulation and transport treat similarly all particles, independently of their mixing states. Under the dynamic approach, the mass transfer rate varies with particle composition during condensation/evaporation, leading to differences in PM concentrations between the IM and MSR simulations. Because only the condensation/evaporation of inorganics is computed dynamically here, the differences of $PM_{2.5}$ concentrations between the IM and MSR simulations are relatively low. Because organics may not be at thermodynamic equilibrium [*Couvidat and Sartelet*, 2015] and because they make a significant part of the total particle mass, larger differences would be expected if the condensation/evaporation of organics is computed dynamically.

3.2. Inorganic Aerosol Formation

The impact of the mixing state assumption and the condensation/evaporation approach on the formation of inorganic aerosols is studied here, with a focus on nitrate and ammonium. The sodium and sulphate concentrations are found to be very similar for all simulations, because they are not volatile (with an averaged concentration of 0.165 μg m^{-3} for sodium and 3.11 μg m^{-3} for sulphate). Chloride is ignored in the comparison because its concentration is very small.

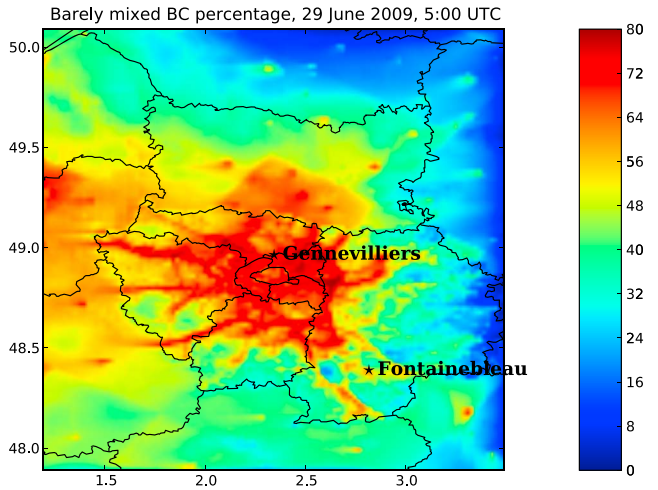

Figure 5. Spatial distribution of the percentage of total BC mass that is in particle class BC (composition index 3) over Paris region.

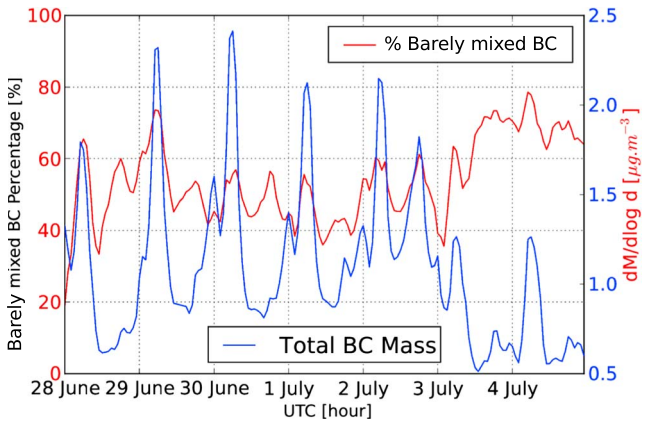

Figure 6. Temporal distribution of BC mixing state over Paris region.

Figure 4 compares the time evolution of nitrate (NO_3) and ammonium (NH_4) between the four simulations at Gennevilliers. For both the MSR and the IM simulations, the dynamic approach for condensation/evaporation leads to lower peaks and higher troughs for NO_3, but higher peaks and lower troughs for NH_4, compared to the bulk equilibrium approach. Similarly to the $PM_{2.5}$ concentration results, if bulk equilibrium is assumed for condensation/evaporation, the mixing state assumption makes almost no difference on both NO_3 concentrations (0.88 μg m^{-3} in average) and NH_4 (1.19 μg m^{-3} in average). Using the dynamic approach for condensation/evaporation, MSR leads to higher NO_3 concentrations (1.24 μg m^{-3} in average) than IM (0.76 μg m^{-3} in average) and lower NH_4 concentrations (1.23 μg m^{-3} in average) than IM (1.33 μg m^{-3} in average). Furthermore, the differences are especially high for peak concentrations. Between 3 and 4 July, the peak concentration of NO_3 for the MSR simulation is twice the one for the IM simulation. Using the dynamic approach, the impact of the mixing state assumption is larger (average difference of 0.48 μg m^{-3} for NO_3 and 0.1 μg m^{-3} for NH_4) than the impact of the condensation/evaporation approach (average difference of 0.35 μg m^{-3} for NO_3 and 0.04 μg m^{-3} for NH_4 with MSR).

Because sulphate concentrations do not change between the IM and MSR simulations, an increase of NO_3 would lead to an increase of NH_4 if bulk equilibrium is considered for condensation/evaporation. However, in the MSR simulations, NH_4 decreases because the amount neutralized by sulphate is lower than that in the IM simulations. This leaves more ammonia available to react with nitric acid, leading to an increase of NO_3. The differences in NO_3 and NH_4 between the MSR and IM simulations are caused by the dynamic partitioning between the gas and the particle phases with different surface equilibrium concentrations in the MSR and IM simulations. For a better understanding, let us define [TA], [TS], and [TN] as the total (gas + particle) molar concentrations of ammonium, sulphate, and nitrate, respectively. Two different chemical environments around particle surface may exist. If [TA] > 2 [TS], then the local environment is ammonia rich, and all sulphate is in the form of $(NH_4)_2SO_4$. On the contrary, if [TA] < 2 [TS], then the environment is ammonia-poor, sulphate is not fully neutralized and it may be in the form of both $(NH_4)_3H(SO_4)_2$ and $(NH_4)_2SO_4$. Because $(NH_4)_3H(SO_4)_2$ has lower NH_4 to SO_4 ratio than $(NH_4)_2SO_4$, less NH_4 is formed in ammonia-poor environment than in ammonia-rich environment. In the IM simulation, within a size section, the mass of sulphate is the same for each particle, and each particle neutralizes the same amount of ammonia. Once sulphate is fully neutralized, then the remaining ammonia reacts with nitric acid to condense, which means that ammonium nitrate can only be formed under an ammonia-rich environment. However, in the MSR simulation, particles may contain different amounts of sulphate. For particles that contain a high fraction of sulphate, the local environment may be ammonia poor, reducing the amount of ammonium neutralized by sulphate compared to the IM simulation and increasing the amount of ammonia available for particles that contain a low fraction of sulphate. For those particles, more ammonia is left in the gas phase after neutralization of sulphate, favoring the formation of NH_4NO_3 and leading to more nitrate in the particulate phase than in the IM simulation.

3.3. Mixing State of BC

The SCRAM model provides the opportunity to investigate particle mixing state. As BC is an inert component of particles and as it is the most strongly light-absorbing one, the mixing state of BC is studied here, using the MSR simulation with the dynamic approach.

We define the barely mixed BC percentage as the ratio of the BC mass of barely mixed BC particles (composition index 3 in Table 2) to the BC mass of all particles. Figure 5 shows the spatial distribution of the barely mixed BC percentage during the morning rush hour at 5:00 A.M. UTC on 29 June 2009. Regions with strong traffic emissions have high barely mixed BC percentages, such as the highways and ring roads around the city. Up to 80% of the BC mass may be barely mixed. Figure 6 shows the time evolution of the total BC mass as well as the barely mixed BC percentage at an urban site Gennevilliers. A good correlation can be found

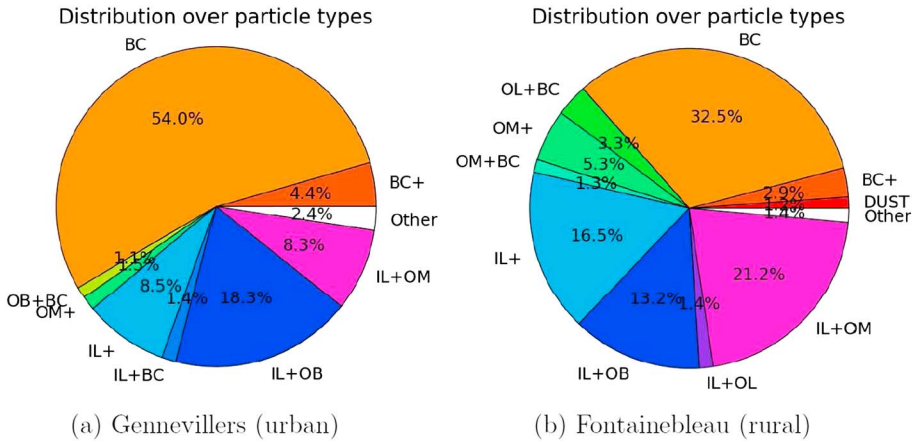

Figure 7. Comparison between partitioning of BC mass among the particle types at urban and rural site (week averaged at ground level).

between the peaks of BC mass concentrations and peaks of barely mixed BC percentages during the morning rush hours. Peaks of barely mixed BC percentages are also observed in the late afternoon during the evening rush hours, although the increase of the total BC mass during the evening rush hours is low. Between 28 June and 3 July, the barely mixed BC percentage does not drop to low values: it is higher than 35% with a peak at 72%. Between 3 and 4 July, the barely mixed BC percentage increases to values above 60% with a peak at 80%. This is caused by a strong wind event on 3 July, which clears out most of the background particles and the total BC mass is lower than that between 28 June and 3 July. The same decrease can also be observed in the time evolution of $PM_{2.5}$ in Figure 3. Particles are therefore less mixed on 3 and 4 July than between 28 June and 3 July.

The BC mixing state at an urban and rural sites is compared in Figure 7, which presents the week-averaged partition of BC mass among the particle types at both the urban site of Gennevilliers and the rural site of Fontainebleau (48.35°N, 2.77°E) (southeast of Paris, see Figure 5). At the urban site, more than half (53.8%) of the total BC mass is barely mixed on average, whereas at the rural site, only 32.2% of the total BC mass is barely mixed. BC particles are more mixed at the rural site, because it is farther apart from emission sources, such as traffic emissions. At both the urban and the rural sites, a large percentage of mixed BC particles contains inorganic species (IL), which are often mixed with organics (IL+OB, IL+OL, and IL+OM). A larger percentage of BC particles are mixed with organics (9.7% of OM+, OM+BC, and OL+BC) at the rural site than at the urban site (2.5% of OM+ and OB+BC). This is a result of a higher ratio between secondary organic aerosols (SOA) concentrations and BC concentration: the SOA/BC ratio is 3.6 at the rural site and 2.3 at the urban site (2.3).

4. Aerosol Optical Properties

Particles attenuate the solar radiation, influencing the earth radiative budget and affecting the climate. This attenuation is modeled using aerosol optical properties, such as the Aerosol Optical Depth or Thickness (AOD/AOT) and the Single Scattering Albedo (SSA). The AOD represents the attenuation of solar radiation, while the SSA represents the importance of scattering during such attenuation. Both the AOD and SSA values are determined by the vertical particle concentrations. They depend on the size, the composition, and the mixing state of particles. In this section, the computation of aerosol optical properties is first detailed. The AOD values are then compared to AERONET measurements, and the influence of the mixing state assumption is studied. Finally, the particle types that contribute the most to high AOD values are determined. AODs and SSAs are computed from the concentrations of both the IM and MSR simulations with the dynamic approach (AOD_{int} and AOD_{ext}; SSA_{int} and SSA_{ext}).

4.1. Computation of Aerosol Optical Properties

Different chemical species have different abilities to scatter or absorb radiations, and such information is usually represented by the Complex Refractive Index (CRI). The CRI is sensitive to the wavelength of incident light. In this study, the optical properties at 550 nm are investigated. Table 4 shows the CRI used in this study. They are obtained from the ADIENT/APPRAISE technical report (http://www.met.rdg.ac.uk/~adient) for inorganics

Table 4. CRI of Simulated Species at $\lambda = 550$ nm in Dry State

Species	Real	Imaginary
Nitrate	1.60	0.0
Ammonium	1.53	-6.0×10^{-3}
Sulphate	1.53	0.0
Sodium	1.50	-1.0×10^{-8}
Chloride	1.50	-1.0×10^{-8}
BC	1.95	−0.79
Mineral dust	1.52	-1×10^{-3}
Hydrophilic organics	1.53	-6.0×10^{-3}
Hydrophobic organics	1.53	-8.0×10^{-3}

and from the OPAC software package [*Hess et al.*, 1998] for organics (water soluble type for hydrophilic organics and insoluble for hydrophobic organics).

Because particles are often made of several chemical components, an Aerosol Complex Refractive Index (ACRI) is determined from the CRI. Two methods may be used to do so: one method assumes that the chemical components are well mixed, and the other assumes that BC is a nonmixed core at the center of each BC containing particles. In the first method, the ACRI is computed by a simple volume-averaged procedure. The second method uses the Maxwell-Garnett approximation [*Maxwell Garnett*, 1904]. After computing the ACRI value m, the extinction and the scattering coefficients are computed based on the Mie theory [*Mie*, 1908], using the Mie code of *Bohren and Huffman* [1983]. Although observations [*Li et al.*, 2011] show that particles may neither be homogeneously mixed nor have a core-shell structure, results of both methods are presented here for comparison. Finally, the AOD and the aerosol scattering depth (ASD) at a wavelength λ are calculated as the integral of the extinction coefficient and the scattering coefficient respectively through the vertical of atmosphere. The single scattering albedo (SSA) is defined by $\frac{\text{ASD}}{\text{AOD}}$. The algorithm for computing the AOD and aerosol optical properties is obtained from *Tombette et al.* [2008] and *Wang et al.* [2014].

4.2. Comparisons to AERONET Measurements

AERONET (AErosol RObotic NETwork) is a ground-based remote sensing network, with aerosol optical measurements performed by Sun photometers [*Holben et al.*, 1998]. Its database provides accurate AOD measurements at different wavelengths, with a measurement uncertainty lower than 0.02 [*Holben et al.*, 2001]. Three data quality levels are available: level 1.0 (unscreened), level 1.5 (cloud screened), and level 2.0 (cloud screened and quality assured). Three AERONET stations are available over Greater Paris: one urban station Paris (48.87°N, 2.33°E; 50 m above sea level (asl)) and two suburban stations Palaiseau (48.70°N, 2.21°E; 156 m asl) and Créteil (48.78°N, 2.44°E; 59 m asl) (marked in Figure 9). In this study, level 2.0 AOD data at 500 and 675 nm are used to derive AOD_{obs} data at 550 nm following the Ångström law:

$$\text{AOD}(550) = \text{AOD}(500) \times \left(\frac{550}{500}\right)^{-\alpha} \tag{1}$$

with α the Ångström exponent:

$$\alpha = \ln\left(\frac{\text{AOD}(500)}{\text{AOD}(675)}\right) / \ln\left(\frac{675}{500}\right). \tag{2}$$

Table 5. Statistics Between AOD Values Computed From Simulation Results and the Measurements of the AERONET[a]

Simulations	Obs. Mean	Sim. Mean	RMSE	Corr.	MFB	MFE
IM-core	0.30	0.28	0.18	49.3%	−14.4%	38.7%
IM-mix	0.30	0.29	0.18	48.2%	−11.9%	37.8%
MSR-core	0.30	0.28	0.18	49.2%	−16.1%	39.3%
MSR-mix	0.30	0.28	0.18	48.3%	−13.6%	38.2%

[a](Obs. stands for observation. Sim. stands for simulation. Corr. stands for correlation.)

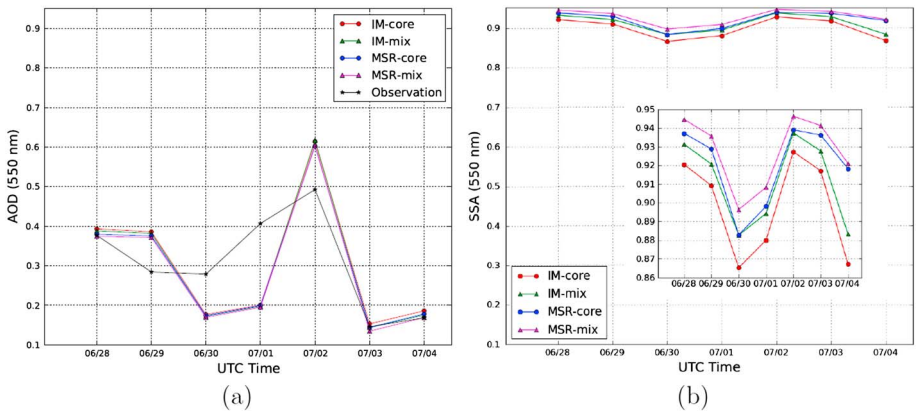

Figure 8. (a) Comparison of AOD between different mixing assumptions and the observation; (b) comparison of SSA between IM and MSR case; Both plots are based on the data collected from the location of AERONET site Paris (48.87°N, 2.33°E; 50 m asl).

Table 5 presents the statistics of the comparison of computed AOD values to AERONET measurements at the three available stations. IM-core and MSR-core denote results of the IM and MSR simulations, respectively, with AOD computed using the BC core hypothesis. IM-mix and MSR-mix denote results of the IM and MSR simulations, respectively, with AOD computed using the well-mixed hypothesis. The statistics of results with different mixing states (IM-core, MSR-core, IM-mix, and MSR-mix) are similar. Simulated AODs compare well to measurements, with a mean simulated value of 0.28 and a mean observed value of 0.30. The correlations are between 48% and 50%. The MFB and MFE values satisfy the model performance goal criterion of *Boylan and Russell* [2006]. Figure 8 shows the daily variations of AOD and SSA at the urban station Paris. AOD values are very similar for IM-core, MSR-core, IM-mix, and MSR-mix, and the daily variations compare well to observations. Both the simulated and the observed AOD are the highest in 2 July and the lowest in 30 June. Higher differences between the results of different mixing states are observed for SSA at the station Paris. The next section studies in more details the influence of the mixing state on AOD and SSA at the station Paris and over the domain of study (Greater Paris).

4.3. Influence of the Mixing State

Because the AERONET station Paris is located downtown Paris where particles and especially BC are largely barely mixed, it is a good location to study the influence of the particle mixing state on AOD and SSA. By comparing the absolute difference between four cases in Figure 8, it can be found that the influence of the mixing state is larger on SSA than on AOD at Paris. Using the same AOD computation method (core or mix), the IM simulation leads to higher AOD values and lower SSA values than the MSR simulation. However, for the same mixing state assumption in the simulation, the BC core hypothesis in the AOD computation method leads to slightly lower AOD and higher SSA than the well-mixed hypothesis. However, the differences are lower than the differences between the MSR and IM simulations using the same AOD computation method.

The higher SSA values observed for MSR BC particles are explained by the fact that for a given mass of BC within a particle, its absorption cross section is greater when other nonabsorbing materials are also present than when the particle is made of pure BC. Hence, as discussed in *Seinfeld and Pandis* [1998], in the MSR simulations, BC is highly concentrated in several BC-dominated particle types, while BC is present in all particles in the IM simulations, leading to larger total absorption cross sections and larger absorption effects.

The influence on SSA is in good agreement with the results of *Mallet et al.* [2004], which indicate that IM reduces SSA by about 15% compared to MSR. The SSA difference between different mixing assumptions is lower in this study than in *Mallet et al.* [2004], because in *Mallet et al.* [2004] SSA is computed by assuming that BC is either completely mixed or not mixed at all with other components. However, in our MSR simulations, BC can have different mixing states (see section 3.3).

Figure 9 shows the spatial distribution of the weekly averaged AOD and SSA differences between the IM and MSR simulations with the well-mixed hypothesis for optical calculations. Using the BC core rather than the well-mixed hypothesis leads to sightly lower differences for AOD and SSA between the IM and MSR simulations

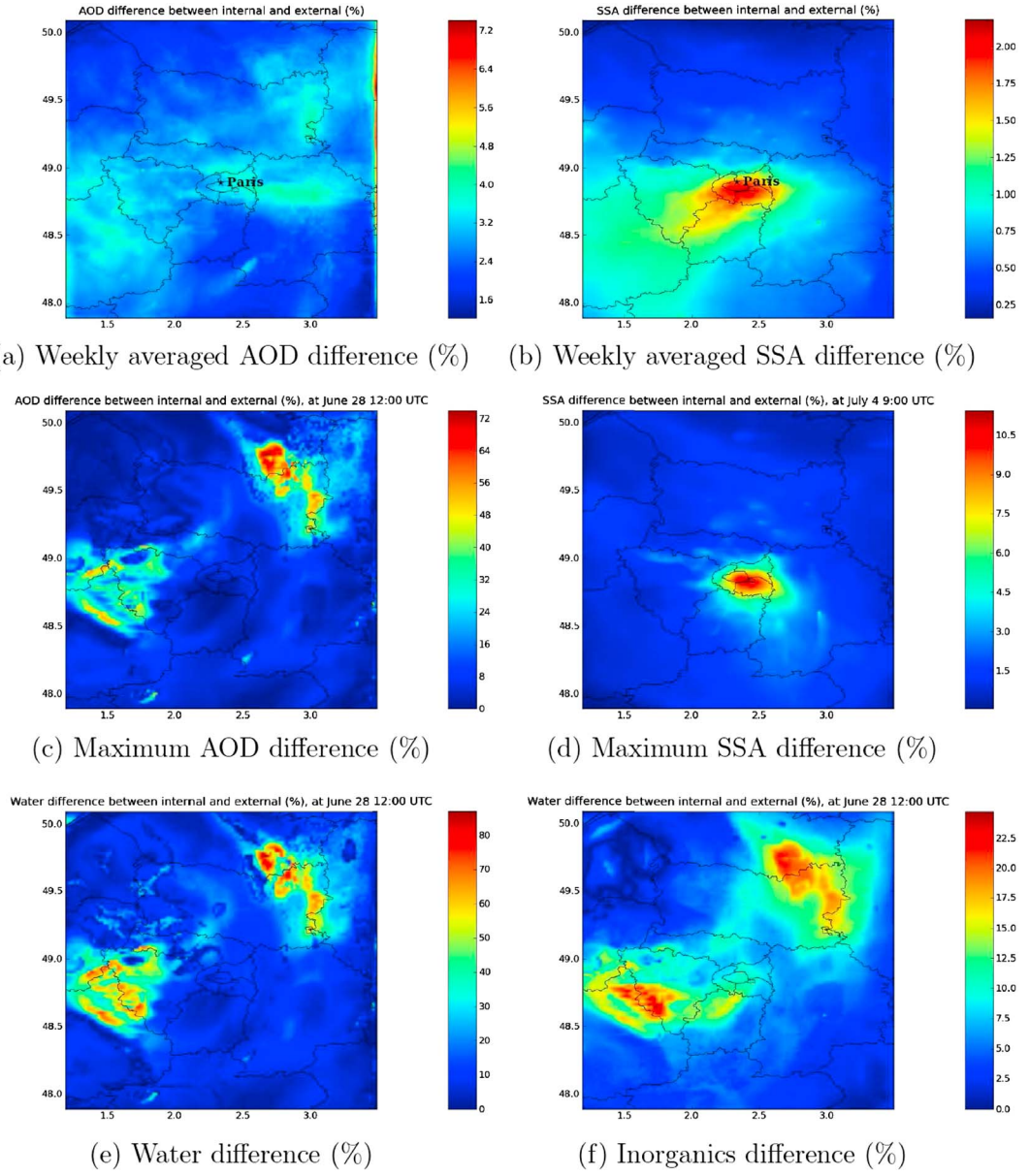

Figure 9. Spatial distributions of differences between different mixing assumptions of different parameters.

(about 2.0% lower for AOD and about 0.7% lower for SSA). AOD and SSA differences are calculated using the following equation:

$$\text{Difference} = \left| \frac{\omega_{\text{MSR}} - \omega_{\text{IM}}}{\omega_{\text{IM}}} \right| \times 100\% \tag{3}$$

where ω_{IM} and ω_{MSR} are either AOD or SSA obtained from the IM and MSR simulations, respectively. For SSA, the larger differences between IM and MSR are concentrated in the city of Paris, where a large percentage of BC is barely mixed in the MSR simulation, affecting the absorption and scattering properties of particles. Although, on average, over the week of simulation, the highest SSA difference is only 2.15%, Figure 9d shows that for specific time periods (e.g., during rush hour at 9:00 A.M. on 4 July when 80% of BC is barely mixed) the difference can be as high as 10.7%. For AOD, differences between IM and MSR are rather low over the city of Paris, but they are high over some regions such as the northeast and the southwest of Paris. Although the weekly averaged AOD difference is at most 7.25%, the hourly averaged difference can be as high as 72.5%, for example, at 12:00 A.M. on 28 June (see Figure 9c). The differences in AOD are mostly related to differences in mass concentrations between the IM and MSR simulations. Water plays an important role in light

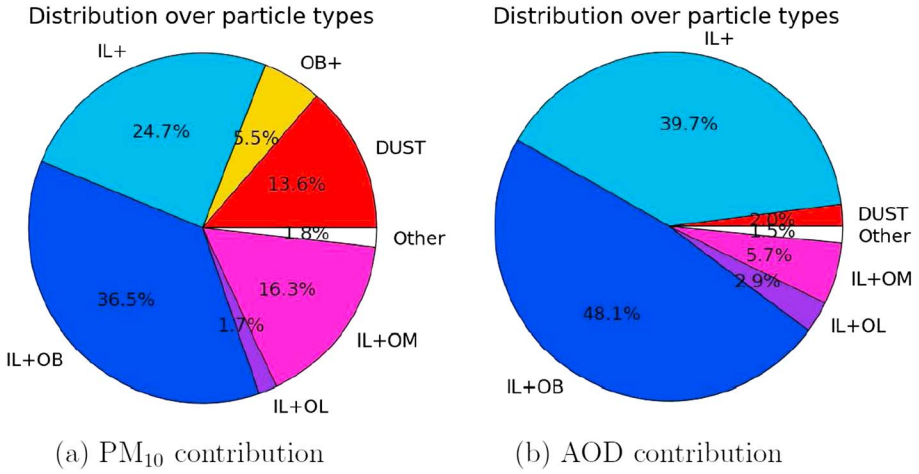

Figure 10. (a) Averaged mass fractions of each particle type (all level); (b) averaged AOD fraction contributed by each particle type.

scattering and the AOD differences are mostly caused by difference of aerosol water content. Indeed, the comparison of Figures 9c and 9e shows that the AOD difference is strongly correlated to difference in aerosol water concentration. The aerosol water content used in the optical computation is computed based on inorganic concentrations using ISORRPIA (organics do not contribute here to water uptake). Therefore, the water concentration differences originate in differences of inorganic concentrations, as shown by the comparison of Figures 9e and 9f where water concentration differences and inorganic concentrations differences are spatially correlated. Such differences of inorganic concentrations originate in differences of ammonium and nitrate concentrations, because of different mixing-state assumptions as discussed in section 3.2. As shown in Figures 9(e) and 9(f), a difference of 22% in inorganic concentrations can lead to differences as high as 80% in water concentration and 72% in AOD.

4.4. Contributions of Particle Types

Figure 10 compares the contribution of each particle type to PM_{10} and AOD. Particles containing inorganic species (IL+OB and IL+) are the main contributors to AOD, with a contribution fraction of 88%. Their contribution to PM_{10} is lower (60%). Moreover, there are only three particle types whose AOD contribution exceeds their mass contribution: IL+, IL+OB, and IL+OL. Let us define the ratio between the AOD contribution fraction (AOD_{frac}) and the PM_{10} contribution fraction (PM_{frac}) as the AOD contribution efficiency (AOD_{eff}) of one particle type: $AOD_{eff} = \frac{AOD_{frac}}{PM_{frac}} \times 100\%$. The IL+OL particles have the highest AOD contribution efficiency (170.6%), followed by the IL+ particles (160.7%), and the IL+OB particles (131.8%). This is a consequence of the hygroscopic property of particles. For a given dry particle diameter, hydrophilic particles have a larger water concentration than hydrophobic particles, thus larger wet diameter, leading to higher particle scattering ability. Therefore, the particle types with the three highest AOD contribution efficiencies contain inorganic hydrophilic species and the particle type containing both inorganics and hydrophilic organics (IL+OL) has the highest AOD contribution efficiency. The contribution of barely mixed BC particle is not large enough to be seen in Figure 9b, as it only processes 0.45% of the total PM mass. However, due to its strong light-absorbing characteristic, it contributes to around 2.1% of the total light absorption caused by aerosols.

5. Cloud Condensation Nuclei

Cloud condensation nuclei (CCN) are particles which have the potential to be activated as cloud droplets. They play an important role in both cloud formation and indirect aerosol forcing [*Seinfeld and Pandis*, 1998]. Based on Köhler equation [*Khöler*, 1921, 1926], the CCN activation is related to both particle wet diameter (Kelvin effect) and composition (solute effect). Because the mixing state of particles influences the particle composition and water content as seen in the previous section, its impact on the formation of CCN may be important. This section first explains briefly the activation of particles as CCN. Then, the impact of the mixing state on the formation of CCN is studied, as well as the contribution of the different particle types to the CCN formation.

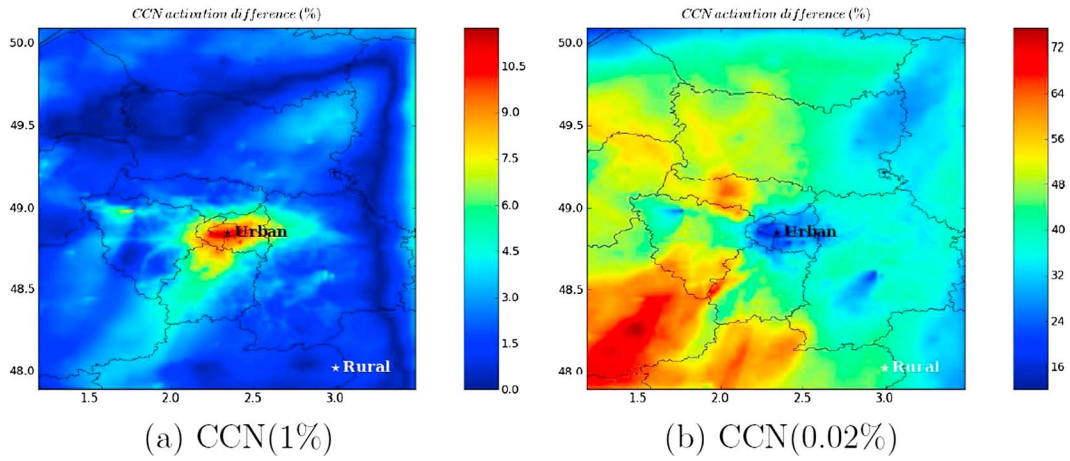

Figure 11. Spatial distributions of weekly averaged CCN activation percentage differences (%) between IM and MSR under (a) high supersaturation (1%) and (b) low supersaturation (0.02%).

5.1. Computation of CCN

A particle is activated into a cloud droplet when the supersaturation of its surrounding environment is larger than a critical supersaturation s_c, which depends on the size and the composition of the particle [*Seinfeld and Pandis*, 1998]:

$$s_c = \exp\left[\left(\frac{4A^3\rho_w M_s}{27\nu\rho_s M_w d_s^3 f_{vs}}\right)^{1/2}\right] - 1 \tag{4}$$

where $A = \frac{4M_w\sigma_w}{RT\rho_w}$, d_s is the particle dry diameter, f_{vs} is the volume fraction of soluble components, ν is the Van't Hoff factor, which represents the averaged number of ions resulting from the dissociation of one solute molecule, M_s and M_w are the molecular weights of solute and water respectively, ρ_s and ρ_w are their densities, T is the temperature, R is the ideal gas constant, and σ_w the water air surface tension.

In this study, only the species of groups IL and OL are considered as soluble species, others are considered as insoluble. Besides, all organic species are considered as nonelectrolyte and with a Van't Hoff factor of 1. An updated routine of *Morales Betancourt and Nenes* [2014] is used for computing the critical supersaturation s_c of particles based on their size and composition. As the computation of CCN is very sensitive to particle size, each size section is divided into 10 size sections of same composition to obtain a smooth CCN spectrum. The new size sections for CCN computation are divided logarithmically within the original size sections (which are also divided logarithmically between 0.01 and 10 μm). So in total 50 size sections are used during the CCN computation and original number and mass concentration redistributed in the new size section using linear interpolation. The number of CCN is computed at six hypothetical supersaturation (0.02, 0.05, 0.1, 0.2, 0.5, and 1.0) percent for the whole simulation domain. Then, the CCN activation percentage is computed based on the ratio of the number of particles that have been activated as CCN to the total number of particles.

5.2. Impact of the Mixing State on CCN

To investigate the impact of the mixing state on CCN, CCN activation percentages are computed at different supersaturations for both the IM and MSR simulations. Figure 11 shows the spatial distribution of the differences between the IM and MSR simulations of the absolute value of the weekly averaged CCN activation percentage at a high supersaturation (1%) and at a low supersaturation (0.02%). This CCN activation difference is computed based on equation (3) by replacing ω_{int} and ω_{ext} by the CCN activation percentage computed from the IM and MSR simulations, respectively. The absolute value of the CCN activation percentage difference between the IM and MSR simulations is lower at 1% supersaturation (between 0 and 11%) than at 0.02% supersaturation (between 12 and 75%), because at 1% supersaturation, hydrophobic particles are more easily activated than at 0.02%, reducing the impact of differences of particle compositions. The spatial pattern of the absolute value of the CCN activation percentage difference is also very different at 1% and at 0.02% supersaturations. At 1% supersaturation, high differences are concentrated over Paris and the near vicinity, where they reach up to 11%. However, at 0.02% supersaturation, differences are larger outside Paris over rural area. The differences over urban regions are a consequence of high concentrations of freshly emitted

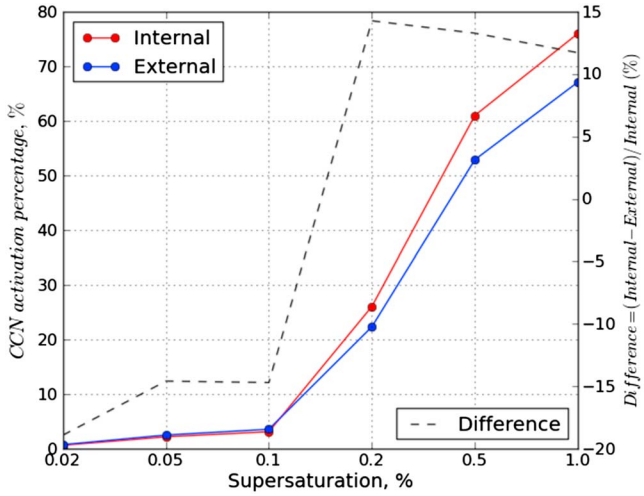

Figure 12. Averaged CCN activation percentage and CCN activation difference (%) for different supersaturation % at an urban site close to center Paris (48.82°N, 2.34°E) as stated in Figure 11a.

insoluble particles such as BC particles from traffic. In the MSR simulation, these particles are hardly activated because they are hydrophobic. However, in the IM simulation, BC is always mixed with hydrophilic components, enhancing the particle activation. Over rural regions, particles are more aged and mixed than over urban regions, leading to a lower percentage of barely mixed hydrophobic BC particles in the MSR simulations. Hence, at high supersaturation, the difference between the MSR and IM simulations is lower than over urban regions and most particles are activated. At low supersaturation, the difference between MSR and IM simulations is high over rural regions, because only particles with very low s_c can be activated, such as large-diameter soluble-rich particles. In the IM simulation, all particles contain both hydrophilic and hydrophobic species, with the hydrophobic components enhancing the activation of particles. However, in the MSR simulations, the particles that are made exclusively of hydrophilic species do get activated.

The relative differences between the IM and MSR simulations are also illustrated in Figure 12, which shows the CCN activation percentage as well as the CCN activation relative difference at six supersaturations at the urban site (48.82°N, 2.34°E) of Figure 11. The relative difference changes sign at around 0.15% supersaturation. Its variations depend on the mass repartition of soluble/insolzuble species over particles, which depends on the mixing state. At low supersaturation, IM leads to lower CCN activation percentage than MSR, because the hydrophobic components of IM particles inhibit activation and only the hydrophilic particles of the MSR simulation may be activated. At high supersaturation, IM leads to higher CCN activation percentage than MSR, because most particles are activated except for the particles that are mostly hydrophobic in the MSR simulation.

5.3. Contribution of Particle Types

Figure 13 compares the relative contribution of the different particle types to the number of CCN activated particles at 0.02% and 1% supersaturations. Inorganic (IL+) particles are activated at lower supersaturation than organic (OM+) particles. At 0.02% supersaturation, the IL+ particles contribute to around 30.5% of the total CCN activation and the fraction of activated organic particles is negligible, while at 1% supersaturation,

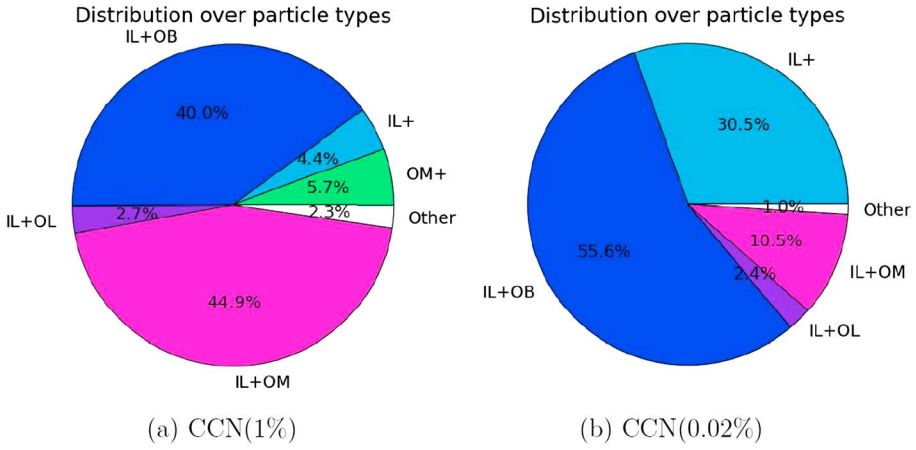

Figure 13. CCN contribution of each particle type under (a) 1% and (b) 0.02% of supersaturation.

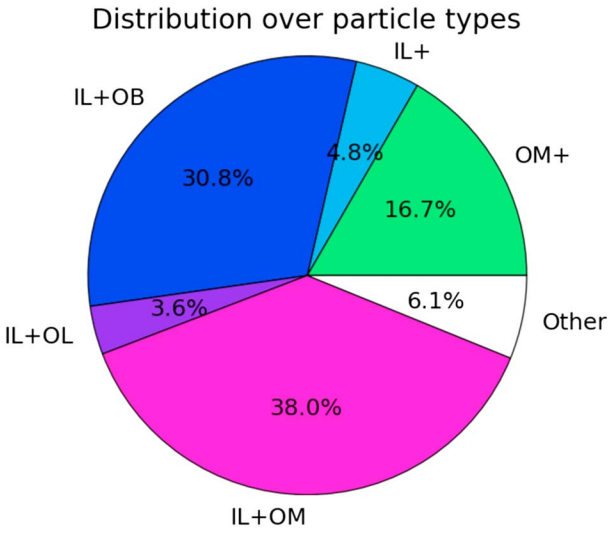

Figure 14. Averaged fraction of each particle type to total aerosol number concentration.

the IL+ contribution is only 4.4%, and almost 6% of activated particles are organic particles (OM+). This is quite reasonable, as IL+ particles are mostly made of soluble materials, thus have low s_c and can easily be activated. At higher supersaturation, a larger percentage of less soluble particles are activated. Thus, the relative contribution IL+ is lower. Moreover, most activated particles contain inorganic species or at least hydrophilic species, as hydrophilic species favor CCN activation. Activated OM+ particles at 1% supersaturation contain more than 20% of hydrophilic species.

The relative contribution of the different particle types to the total aerosol number concentration is presented in Figure 14. There are five particle types that mostly contribute to total number concentration: IL+OM, IL+OB, OM+, IL+, IL+OL. The comparison to Figure 13 shows that these five particle types are activated at 1% supersaturation, while only OM+ is not activated at 0.02% supersaturation. Furthermore, at 1% supersaturation, the comparison shows that the relative contribution of IL+OB and IL+OM to the number of activated particle is higher than their contribution to the total number of particles, while the contribution of IL+ to the number of activated particles is slightly lower than its contribution to the total number of particles. These differences in relative contribution may not be explained by the hydrophilic properties of the species, as particles that contain hydrophobic materials (OB or OM) are less easily activated than particles that do not. These differences in relative contribution are explained by differences in the size distribution of chemical species: a great number (42.7%) of IL+ particles are concentrated in the smallest size section ($d_p < 0.0398$ μm), which is very difficult to be activated, whereas this percentage drops to 9.9% for IL+OB particles and to 19% for IL+OM particles.

6. Conclusions

The size-composition resolved aerosol model (SCRAM) coupled to the Polyphemus air quality platform is evaluated over Greater Paris. Four simulations with different mixing state assumptions (IM or MSR) and condensation/evaporation algorithms (bulk equilibrium or dynamic) are compared. The four simulations model well the total mass of PM_{10} and $PM_{2.5}$ and aerosol optical depths, as assessed from comparisons to observations from the BDQA and AERONET networks.

The concentrations from the IM and MSR simulations are similar when bulk equilibrium is assumed for condensation/evaporation. Comparisons therefore focus on differences from the IM and MSR simulations that arise when condensation/evaporation is computed dynamically. Note that only the condensation/evaporation of inorganics is computed dynamically here. The MSR simulation leads to higher nitrate concentrations (1.24 μg m^{-3} on average) than the IM simulation (0.76 μg m^{-3} on average) and lower ammonium concentrations (1.23 μg m^{-3} on average for the MSR simulation and 1.33 μg m^{-3} for the IM simulation). Furthermore, the differences are especially high for peak concentration. Between 3 and 4 July, the peak concentration of nitrate for the MSR simulation is twice the one for the IM simulation.

We define the barely mixed BC percentage as the ratio of the BC mass of barely mixed BC particles (BC makes more than 80% of the particle mass) to the BC mass of all particles. At the urban site of Paris, the barely mixed BC percentage does not drop to low values: it is higher than 35% with peaks around 80% during rush hours when emissions are the highest.

Detailed analyzes are also conducted to investigate the impact of the mixing state on particle optical properties as well as on the cloud condensation nuclei (CCN) based on the dynamic IM and MSR simulations. Using the same aerosol optical depth (AOD) computation method (core or mix), the IM simulation leads to higher AOD values and lower SSA values than the MSR simulation. However, the differences between AOD computed

using a core or mix method are lower than differences between AOD computed from the IM and MSR simulations. For SSA, the larger differences, up to 11% between the IM and MSR simulations, are concentrated in the city of Paris, where a large percentage of BC is barely mixed in the MSR simulation, affecting the absorption and scattering properties of particles. For AOD, differences between the IM and MSR simulation are rather low over the city of Paris, but they are high over some regions such as the northeast and the southwest of Paris. Differences are due to differences in inorganic concentrations resulting from differences in the mixing state assumption, and leading to differences in water aerosol concentrations, and AOD. For example, a difference of 22% in inorganic concentrations can lead to differences as high as 80% in water concentration and 72% in AOD. Concerning CCN, at low supersaturation, the IM simulation leads to lower CCN activation percentage than the MSR simulation, because the hydrophobic components of IM particles inhibit activation and only the hydrophilic particles of the MSR simulation may be activated. At high supersaturation, the IM simulation leads to higher CCN activation percentage than the MSR simulation, because most particles are activated except for the particles that are mostly hydrophobic in the MSR simulation. Moreover, in case of high supersaturation, the differences in the spatial distributions between the IM and MSR simulations are more significant over urban regions. However, such distribution pattern also inverses at low supersaturation.

Although the potential of SCRAM to investigate particle mixing state has been demonstrated in this study, it is somehow limited as no mixing state observation data are available during our summer simulation period. So the future work will focus on conducting a new simulation where particle-type resolved measurement is available, such as the winter period of 2010 [*Healy et al.*, 2012]. Moreover, the current simulation period is limited to only 1 week due to computational constraints and limited computational resources. Although a comprehensive particle composition discretization has been used in this study, it is still possible to improve such representation. Because most of the particle mass and number are concentrated within a few particle compositions, and several compositions hardly exist during the entire simulation. So it is possible to optimize the computation efficiency by improving the particle class parameterization, which could reduce the total number of particle classes while conserving the particle classes with significant importance.

Acknowledgments

The author would like to thank AERONET for providing AOD measurements (http://aeronet.gsfc.nasa.gov), and the principal investigators of the Paris (Francois Ravetta and Jacques Pelon), Palaiseau (Philippe Goloub), and Créteil (Bernadette Chatenet) stations. Yang Zhang acknowledges funding from the U.S. Department of Energy Office of Science Biological and Environmental Research as part of the Global and Regional Climate Modeling programs (DE-SC0006695). Simulation results and data are available upon request (shupeng.zhu@enpc.fr). The code of Polyphemus and SCRAM are available on the site of CEREA: http://cerea.enpc.fr/en/modeles.html. Both SCRAM and Polyphemus have a GNU (General Public License). The user can redistribute them and/or modify them under the terms of the GNU General Public License as published by the Free Software Foundation. This description has been added after the conclusion.

References

Airparif (2010), Ile-de-France gridded emission inventory 2005 (version 2008).

Aquila, V., et al. (2011), MADE-in: A new aerosol microphysics submodel for global simulation of insoluble particles and their mixing state, *Geosci. Model Dev.*, *4*(2), 325–355.

Bauer, S., D. Wright, D. Koch, E. Lewis, R. McGraw, L.-S. Chang, S. Schwartz, and R. Ruedy (2008), MATRIX (Multiconfiguration Aerosol TRacker of mIXing state): An aerosol microphysical module for global atmospheric models, *Atmos. Chem. Phys.*, *8*(20), 6003–6035.

Bohren, C. F., and D. R. Huffman (1983), *Absorption and Scattering of Light by Small Particles*, Wiley, New York.

Boylan, J. W., and A. G. Russell (2006), PM and light extinction model performance metrics, goals, and criteria for three-dimensional air quality models, *Atmos. Environ.*, *40*(26), 4946–4959.

Couvidat, F., and K. Sartelet (2015), The Secondary Organic Aerosol Processor (SOAP v1. 0) model: A unified model with different ranges of complexity based on the molecular surrogate approach, *Geosci. Model Dev.*, *8*(4), 1111–1138.

Couvidat, F., É. Debry, K. Sartelet, and C. Seigneur (2012), A hydrophilic/hydrophobic organic (H^2O) aerosol model: Development, evaluation and sensitivity analysis, *J. Geophys. Res.*, *117*, D10304, doi:10.1029/2011JD017214.

Couvidat, F., Y. Kim, K. Sartelet, C. Seigneur, N. Marchand, and J. Sciare (2013), Modeling secondary organic aerosol in an urban area: Application to Paris, France, *Atmos. Chem. Phys.*, *13*(2), 983–996.

Davidson, C. I., R. F. Phalen, and P. A. Solomon (2005), Airborne particulate matter and human health: A review, *Aerosol Sci. Technol.*, *39*(8), 737–749.

Debry, E., and B. Sportisse (2006), Reduction of the condensation/evaporation dynamics for atmospheric aerosols: Theoretical and numerical investigation of hybrid methods, *J. Aerosol Sci.*, *37*(8), 950–966.

Dergaoui, H., K. N. Sartelet, É. Debry, and C. Seigneur (2013), Modeling coagulation of externally mixed particles: Sectional approach for both size and chemical composition, *J. Aerosol Sci.*, *58*(0), 17–32.

Fahey, K. M., and S. N. Pandis (2001), Optimizing model performance: Variable size resolution in cloud chemistry modeling, *Atmos. Environ.*, *35*(26), 4471–4478.

Guenther, A., T. Karl, P. Harley, C. Wiedinmyer, P. Palmer, and C. Geron (2006), Estimates of global terrestrial isoprene emissions using MEGAN (Model of Emissions of Gases and Aerosols from Nature), *Atmos. Chem. Phys. Discuss.*, *6*(1), 107–173.

Healy, R., et al. (2012), Sources and mixing state of size-resolved elemental carbon particles in a European megacity: Paris, *Atmos. Chem. Phys.*, *12*(4), 1681–1700.

Healy, R. M., et al. (2013), Quantitative determination of carbonaceous particle mixing state in Paris using single-particle mass spectrometer and aerosol mass spectrometer measurements, *Atmos. Chem. Phys.*, *13*(18), 9479–9496.

Hess, M., P. Koepke, and I. Schult (1998), Optical properties of aerosols and clouds: The software package OPAC, *Bull. Am. Meteorol. Soc.*, *79*(5), 831–844.

Holben, B., et al. (1998), AERONETA federated instrument network and data archive for aerosol characterization, *Remote Sens. Environ.*, *66*(1), 1–16.

Holben, B., A. Smirnov, T. Eck, I. Slutsker, N. Abuhassan, W. Newcomb, J. Schafer, D. Tanre, B. Chatenet, and F. Lavenu (2001), An emerging ground-based aerosol climatology: Aerosol optical depth from AERONET, *J. Geophys. Res.*, *106*(D11), 12,067–12,097.

Hong, S.-Y., Y. Noh, and J. Dudhia (2006), A new vertical diffusion package with an explicit treatment of entrainment processes, *Mon. Weather Rev.*, *134*(9), 2318–2341.

Horowitz, L. W., et al. (2003), A global simulation of tropospheric ozone and related tracers: Description and evaluation of MOZART, version 2, *J. Geophys. Res.*, *108*(D24), 4784, doi:10.1029/2002JD002853.
Jacobson, M. Z. (2001), Strong radiative heating due to the mixing state of black carbon in atmospheric aerosols, *Nature*, *409*(6821), 695–697.
Jacobson, M. Z. (2002a), Analysis of aerosol interactions with numerical techniques for solving coagulation, nucleation, condensation, dissolution, and reversible chemistry among multiple size distributions, *J. Geophys. Res.*, *107*(D19), 4366, doi:10.1029/2001JD002044.
Jacobson, M. Z. (2002b), Control of fossil-fuel particulate black carbon and organic matter, possibly the most effective method of slowing global warming, *J. Geophys. Res.*, *107*(D19), 4410, doi:10.1029/2001JD001376.
Jacobson, M. Z., R. P. Turco, E. J. Jensen, and O. B. Toon (1994), Modeling coagulation among particles of different composition and size, *Atmos. Environ.*, *28*(7), 1327–1338.
Kaiser, J., J. Hendricks, M. Righi, N. Riemer, R. A. Zaveri, S. Metzger, and V. Aquila (2014), The MESSy aerosol submodel MADE3 (v2. 0b): Description and a box model test, *Geosci. Model Dev.*, *7*(3), 1137–1157.
Kim, Y., K. Sartelet, J.-C. Raut, and P. Chazette (2013), Evaluation of the Weather Research and Forecast/urban model over Greater Paris, *Boundary Layer Meteorol.*, *149*(1), 105–132.
Kleeman, M. J., and G. R. Cass (2001), A 3D Eulerian source-oriented model for an externally mixed aerosol, *Environ. Sci. Technol.*, *35*(24), 4834–4848.
Köhler, H. (1921), Zur kondensation des wasserdampfe in der atmosphare, *Geof. Publ.*, *2*(1), 6.
Köhler, H. (1926), *Zur Thermodynamik der Kondensation an hygroskopischen Kernen und Bemerkungen über das Zusammenfliessen der Tropfen*, Statens Meteorologisk-Hydrografiska Anstalt, Stockholm, Sweden.
Lance, S., T. Raatikainen, T. B. Onasch, D. R. Worsnop, X.-Y. Yu, M. Alexander, M. Stolzenburg, P. McMurry, J. N. Smith, and A. Nenes (2013), Aerosol mixing state, hygroscopic growth and cloud activation efficiency during MIRAGE 2006, *Atmos. Chem. Phys.*, *13*(9), 5049–5062.
Leck, N., and E. Svensson (2014), Importance of aerosol composition and mixing state for cloud droplet activation in the high Arctic, *Atmos. Chem. Phys. Discuss.*, *14*(15), 21,223–21,283.
Lesins, G., P. Chylek, and U. Lohmann (2002), A study of internal and external mixing scenarios and its effect on aerosol optical properties and direct radiative forcing, *J. Geophys. Res.*, *107*(D10), doi:10.1029/2001JD000973.
Li, W., P. Li, G. Sun, S. Zhou, Q. Yuan, and W. Wang (2011), Cloud residues and interstitial aerosols from non-precipitating clouds over an industrial and urban area in Northern China, *Atmos. Environ.*, *45*(15), 2488–2495.
Lu, J., and F. M. Bowman (2010), A detailed aerosol mixing state model for investigating interactions between mixing state, semivolatile partitioning, and coagulation, *Atmos. Chem. Phys.*, *10*(8), 4033–4046.
Mallet, M., J. Roger, S. Despiau, J. P. Putaud, and O. Dubovik (2004), A study of the mixing state of black carbon in urban zone, *J. Geophys. Res.*, *109*, D04202, doi:10.1029/2003JD003940.
Mallet, V., et al. (2007), Technical Note: The air quality modeling system Polyphemus, *Atmos. Chem. Phys.*, *7*(20), 5479–5487.
Matsui, H., M. Koike, Y. Kondo, J. D. Fast, and M. Takigawa (2014), Development of an aerosol microphysical module: Aerosol Two-dimensional bin module for foRmation and Aging Simulation (ATRAS), *Atmos. Chem. Phys.*, *14*(18), 10,315–10,331.
Maxwell Garnett, J. C. (1904), Colours in metal glasses and metal films, *Philos. Trans. R. Soc. London Ser. A*, *3*, 385–420.
Mie, G. (1908), Beitrage zur Optik trüber Medien, speziell kolloidaler Metallösungen, *Ann. Phys.*, *330*(3), 377–445.
Morales Betancourt, R., and A. Nenes (2014), Droplet activation parameterization: The population-splitting concept revisited, *Geosci. Model Dev.*, *7*(5), 2345–2357.
Murphy, D. M., D. J. Cziczo, K. D. Froyd, P. K. Hudson, B. M. Matthew, A. M. Middlebrook, R. E. Peltier, A. Sullivan, D. S. Thomson, and R. J. Weber (2006), Single-particle mass spectrometry of tropospheric aerosol particles, *J. Geophys. Res.*, *111*, D23S32, doi:10.1029/2006JD007340.
Nenes, A., S. N. Pandis, and C. Pilinis (1998), ISORROPIA: A new thermodynamic equilibrium model for multiphase multicomponent inorganic aerosols, *Aquat. Geochem.*, *4*(1), 123–152.
Oshima, N., M. Koike, Y. Zhang, Y. Kondo, N. Moteki, N. Takegawa, and Y. Miyazaki (2009), Aging of black carbon in outflow from anthropogenic sources using a mixing state resolved model: Model development and evaluation, *J. Geophys. Res.*, *114*, D06210, doi:10.1029/2008JD010680.
Pascal, M., et al. (2013), Assessing the public health impacts of urban air pollution in 25 European cities: Results of the Aphekom project, *Sci. Total Environ.*, *449*, 390–400.
Riemer, N., M. West, R. A. Zaveri, and R. C. Easter (2009), Simulating the evolution of soot mixing state with a particle-resolved aerosol model, *J. Geophys. Res.*, *114*, D09202, doi:10.1029/2008JD011073.
Russell, L. M., and J. H. Seinfeld (1998), Size-and composition-resolved externally mixed aerosol model, *Aerosol Sci. Technol.*, *28*(5), 403–416.
Sartelet, K., E. Debry, K. Fahey, Y. Roustan, M. Tombette, and B. Sportisse (2007), Simulation of aerosols and gas-phase species over Europe with the POLYPHEMUS system: Part I Model-to-data comparison for 2001, *Atmos. Environ.*, *41*(29), 6116–6131.
Sarwar, G., D. Luecken, G. Yarwood, G. Z. Whitten, and W. P. Carter (2008), Impact of an updated carbon bond mechanism on predictions from the CMAQ modeling system: Preliminary assessment, *J. Appl. Meteorol. Climatol.*, *47*(1), 3–14.
Seinfeld, J. H., and S. N. Pandis (1998), *Atmospheric Chemistry and Physics: From Air Pollution to Climate Change*, 2nd ed., 1248 pp, John Wiley, Hoboken, N. J.
Skamarock, W., J. Klemp, J. Dudhia, D. Gill, and D. Barker (2005), Coauthors, 2008: A description of the Advanced Research WRF version 3. NCAR Tech, *Tech Rep., Note NCAR/TN-4751STR*.
Stier, P., et al. (2005), The aerosol-climate model ECHAM5-HAM, *Atmos. Chem. Phys.*, *5*(4), 1125–1156.
Tombette, M., P. Chazette, B. Sportisse, and Y. Roustan (2008), Simulation of aerosol optical properties over Europe with a 3-D size-resolved aerosol model: Comparisons with AERONET data, *Atmos. Chem. Phys.*, *8*(23), 7115–7132.
Vehkamäki, H., M. Kulmala, I. Napari, K. E. J. Lehtinen, C. Timmreck, M. Noppel, and A. Laaksonen (2002), An improved parameterization for sulfuric acid–water nucleation rates for tropospheric and stratospheric conditions, *J. Geophys. Res.*, *107*(D22), 4622, doi:10.1029/2002JD002184.
Vogel, B., H. Vogel, D. Bäumer, M. Bangert, K. Lundgren, R. Rinke, and T. Stanelle (2009), The comprehensive model system COSMO-ART—Radiative impact of aerosol on the state of the atmosphere on the regional scale, *Atmos. Chem. Phys.*, *9*(22), 8661–8680.
Wang, Y., K. N. Sartelet, M. Bocquet, and P. Chazette (2014), Modelling and assimilation of lidar signals over Greater Paris during the MEGAPOLI summer campaign, *Atmos. Chem. Phys.*, *14*(7), 3511–3532.
Wex, H., G. McFiggans, S. Henning, and F. Stratmann (2010), Influence of the external mixing state of atmospheric aerosol on derived CCN number concentrations, *Geophys. Res. Lett.*, *37*, L10805, doi:10.1029/2010GL043337.
Zhang, H., S. DeNero, D. Joe, H.-H. Lee, S.-H. Chen, J. Michalakes, and M. Kleeman (2014), Development of a source oriented version of the WRF/Chem model and its application to the California regional PM 10/PM 2.5 air quality study, *Atmos. Chem. Phys.*, *14*(1), 485–503.
Zhu, S., K. Sartelet, and C. Seigneur (2015), A size-composition resolved aerosol model for simulating the dynamics of externally mixed particles: SCRAM (v 1.0), *Geosci. Model Dev.*, *8*(6), 1595–1612.